

# On the physical mechanisms of two-way coupling in particle-laden isotropic turbulence

A. Ferrante<sup>a)</sup> and S. Elghobashi<sup>b)</sup>

*Department of Mechanical and Aerospace Engineering, University of California, Irvine, California 92697*

(Received 26 August 2002; accepted 30 October 2002; published 7 January 2003)

The objective of the present study is to analyze our recent direct numerical simulation (DNS) results to explain in some detail the main physical mechanisms responsible for the modification of isotropic turbulence by dispersed solid particles. The details of these two-way coupling mechanisms have not been explained in earlier publications. The present study, in comparison to the previous DNS studies, has been performed with higher resolution ( $Re_\lambda=75$ ) and considerably larger number (80 million) of particles, in addition to accounting for the effects of gravity. We study the modulation of turbulence by the dispersed particles while fixing both their volume fraction,  $\phi_v=10^{-3}$ , and mass fraction,  $\phi_m=1$ , for three different particles classified by the ratio of their response time to the Kolmogorov time scale: microparticles,  $\tau_p/\tau_k \ll 1$ , critical particles,  $\tau_p/\tau_k \approx 1$ , large particles,  $\tau_p/\tau_k > 1$ . Furthermore, we show that in zero gravity, dispersed particles with  $\tau_p/\tau_k=0.25$  (denoted here as “ghost particles”) modify the spectra of the turbulence kinetic energy and its dissipation rate in such a way that keeps the decay rate of the turbulence energy nearly identical to that of particle-free turbulence, and thus the two-way coupling effects of these ghost particles would not be detected by examining only the temporal behavior of the turbulence energy of the carrier flow either numerically or experimentally. In finite gravity, these ghost particles accumulate, via the mechanism of *preferential sweeping* resulting in the stretching of the vortical structures in the gravitational direction, and the creation of local gradients of the drag force which increase the magnitudes of the horizontal components of vorticity. Consequently, the turbulence becomes anisotropic with a reduced decay rate of turbulence kinetic energy as compared to the particle-free case. © 2003 American Institute of Physics. [DOI: 10.1063/1.1532731]

## I. INTRODUCTION

Understanding the physical mechanisms of the two-way interaction between dispersed particles and the turbulence in simple homogeneous carrier flows is a prerequisite to the development of mathematical models, including SGS models for LES, for practical flows in complex geometries.

Since isotropic turbulence is the simplest homogeneous turbulent flow, it has been the subject of a number of earlier DNS studies on the effects of particles on isotropic turbulence.<sup>1–5</sup> The objective of the present study is to analyze our recent DNS results to explain in some detail the main physical mechanisms responsible for the modification of isotropic turbulence by dispersed solid particles. The details of these two-way coupling mechanisms have not been explained in earlier publications. In addition, the effects of gravity on the two-way coupling mechanisms are included in our study. The present study, in comparison to the previous DNS studies, has been performed with higher resolution ( $Re_\lambda=75$ ) and with considerably larger number (80 million) of particles. We also show that, in zero gravity, dispersed particles with  $\tau_p/\tau_k=0.25$  (denoted here as “ghost particles”) modify the spectra of the turbulence kinetic energy and its dissipation rate in such a way that keeps the decay

rate of the turbulence energy nearly identical to that of particle-free turbulence; thus, the two-way coupling effects of these ghost particles would not be detected, e.g., in microgravity environment, by examining only the temporal behavior of the turbulence energy of the carrier flow either numerically or experimentally.

The paper is organized as follows. The mathematical description is presented in Sec. II including the governing equations in Sec. II A and the numerical method in Sec. II B. The results are discussed in Sec. III including the turbulence and particles parameters in Sec. III A and the physical mechanisms of the two-way coupling in Sec. III C. The summary is presented in Sec. IV.

## II. MATHEMATICAL DESCRIPTION

### A. Governing equations

The governing dimensionless equations for a particle-laden incompressible isotropic turbulent flow are the Navier–Stokes equations

$$\frac{\partial u_j}{\partial t} + \frac{\partial(u_j u_k)}{\partial x_k} = -\frac{\partial p}{\partial x_j} + \nu \frac{\partial^2 u_j}{\partial x_k \partial x_k} - f_j, \quad (1)$$

and the continuity equation

$$\frac{\partial u_j}{\partial x_j} = 0, \quad (2)$$

<sup>a)</sup>Electronic mail: ferrante@eng.uci.edu

<sup>b)</sup>Electronic mail: selghoba@uci.edu

TABLE I. Flow parameters (dimensionless) at initial time ( $t=0$ ), injection time ( $t=1$ ), and for case A at time  $t=5$ .

$t$	$u_0$	$\varepsilon$	$l$	$\lambda$	$\eta$	$Re_l$	$Re_\lambda$	$l/\eta$	$\tau_k$	$\tau_l$
0.0	0.0503	$7.4 \times 10^{-4}$	0.0684	0.0345	0.002 02	150	75	33.8	0.177	1.36
1.0	0.0436	$9.8 \times 10^{-4}$	0.0685	0.0259	0.001 88	129	49	36.4	0.154	1.57
5.0	0.0233	$2.0 \times 10^{-4}$	0.0891	0.0305	0.002 80	90	31	31.9	0.338	3.83

where  $j=1,2,3$  for the three coordinate directions  $x_1, x_2$ , and  $x_3$ , and  $\nu$  is the dimensionless kinematic viscosity.  $-f_j$  is the net force per unit mass of fluid exerted in the  $x_j$  direction by  $M$  particles within the integration control volume, and is computed from

$$f_j = \frac{1}{m_f} \sum_{p=1}^M f_{jp}, \quad (3)$$

where  $f_{jp}$  is the drag force acting on particle  $p$  in the  $x_j$  direction, and  $m_f$  is the mass of fluid within the integration control volume.

The particle equation of motion, derived by Maxey and Riley,<sup>6</sup> can be written for large ratio ( $\rho_p/\rho$ ) of the particle density to fluid density as

$$m_p \frac{dv_j}{dt_p} = m_p \frac{(u_j - v_j)}{\tau_p} + (m_p - m_f)g_j, \quad (4)$$

where  $m_p$  is the mass of the particle,  $d/dt_p$  is the time derivative following the moving particle,  $v_j$  is the particle instantaneous velocity,  $u_j$  is the instantaneous fluid velocity at the particle location, and  $g_j$  is the gravitational acceleration.  $\tau_p$  is the particle response time, which for Stokes drag law is

$$\tau_p = \frac{d^2}{18\nu} \frac{\rho_p}{\rho}, \quad (5)$$

where  $d$  is the particle diameter.

## B. Numerical method

We performed direct numerical simulation (DNS) to solve the unsteady three-dimensional Navier–Stokes and continuity equations [Eqs. (1) and (2)]. These governing equations were discretized in space in an Eulerian framework using a second-order finite-difference scheme on a uniform staggered mesh of  $(256)^3$  grid points. This grid allows an initial microscale Reynolds number  $Re_{\lambda_0} = 75$ . Time integration was performed via the Adams–Bashforth scheme with a time step  $\Delta t = \Delta x/2$ , where  $\Delta x$  is the grid spacing. The simulations were stopped after 2560 time steps at nondimensional time  $t=5$ . Pressure was treated implicitly and was obtained by solving the Poisson equation in finite-difference form using a combination of a two-dimensional fast Fourier transform (FFT) in the  $x_1x_2$  plane, and Gauss elimination in the  $x_3$  direction. Periodic boundary conditions were imposed in the three directions. More details about the numerical method are given by Gerz *et al.*<sup>7</sup>

The initial velocity field was generated by prescribing the turbulence kinetic energy spectrum  $E(\kappa)$  and ensuring that the initial random velocity field is isotropic, divergence-

free with respect to the discretized form of the continuity equation, and that the velocity cross-correlation spectra,  $R_{ij}(\kappa)$ , satisfy the realizability constraints.<sup>8</sup>

The initial energy spectrum at time  $t=0$  was prescribed via

$$E(\kappa) = \left( \frac{3u_0^2}{2} \right) \left( \frac{\kappa}{2\pi\kappa_p^2} \right) \exp\left( -\frac{\kappa}{\kappa_p} \right), \quad (6)$$

where  $\kappa$  is the wave number,  $\kappa_p$  is the wave number of peak energy, and  $u_0$  is the initial dimensionless rms velocity. In the present work the wave numbers are normalized by the lowest nonzero wave number,  $\kappa_{\min} = 2\pi/L$ , where  $L$  is the length of the computational domain ( $L=1$ ). Prescribing the values of  $\kappa_p$  and  $u_0$  determines  $E(\kappa)$  according to Eq. (6). The dimensionless kinematic viscosity,  $\nu$ , was computed from the prescribed initial microscale Reynolds number,  $Re_{\lambda_0}$ , and the computed initial energy dissipation rate,  $\varepsilon(0)$ . The values of the dimensionless parameters at time  $t=0$  were  $\kappa_p=4$ ,  $u_0=0.0503$ ,  $Re_{\lambda_0}=75$ ,  $\varepsilon(0)=7.4 \times 10^{-4}$ , and  $\nu=2.31 \times 10^{-5}$ . Table I shows dimensionless flow parameters ( $l$  and  $\tau_l$  the integral length and time scales,  $Re_l$  and  $Re_\lambda$  the Reynolds number based on  $l$ ,  $\lambda$  the Taylor microscale,  $\eta$  and  $\tau_k$  the Kolmogorov length and time scales) at times  $t=0, 1$ , and  $5$  for the particle-free flow (case A). The values of the reference length and time scales used in normalizing the above quantities were  $L_{\text{ref}}=0.3733$  m and  $t_{\text{ref}}=0.2144$  s, which are consistent with the value of dimensional kinematic viscosity of the fluid (air)  $\nu_{\text{dim}}=1.50 \times 10^{-5}$  m<sup>2</sup>/s. The accuracy of the computations of the single phase flow has been verified via comparison with the well-known properties of decaying isotropic turbulence, e.g., the asymptotic value of the skewness of the velocity derivative, the decay rate of turbulence kinetic energy (TKE), and spectra of TKE and its dissipation rate. In addition, the smallest scales of turbulence are well resolved as indicated by  $\eta\kappa_{\max} \geq 1$  at all times, where  $\kappa_{\max} = 2\pi N/2$  is the maximum resolved wave number and  $N=256$  is the number of grid points in each direction in our computational grid.

Particles were released with a random distribution in the computational domain at time  $t=1$ , when the skewness of the velocity derivative  $S_u$  has reached the value  $-0.50$ , indicating an established nonlinear energy transfer across the spectrum. The time  $t=1$  will be referred to hereinafter as the “injection time,”  $t_{\text{inj}}$ . The initial velocity at  $t_{\text{inj}}$  of each particle was set equal to the instantaneous fluid velocity at the particle position. Particles trajectories were then tracked in time. It should be emphasized that, in decaying turbulence, the prescription of different initial conditions for the particles will have an impact on the two-way coupling effects. A de-

TABLE II. Particle properties (dimensionless) at injection time ( $t=1$ ) with  $\phi_v=10^{-3}$  and  $\phi_m=1.0$  (for  $\rho_p/\rho=1000$ ).

Case	$\tau_p$	$\tau_p/\tau_l$	$\tau_p/\tau_k$	$d$	$d/l$	$d/\eta$	$d(\mu\text{m})$	$M_c$	$M_r/M_c$	$\text{Re}_{p,\text{max}}$	$v_t/u_0^*$
A	...	...	...	...	...	...	...	...	0	...	...
B	0.0154	0.0098	0.1	$0.80 \times 10^{-4}$	0.001 17	0.043	30	$80 \times 10^6$	46.7	0.11	0.0
C	0.0385	0.0245	0.25	$1.26 \times 10^{-4}$	0.001 85	0.067	47	$80 \times 10^6$	11.8	0.31	0.0
D	0.1540	0.0979	1.0	$2.53 \times 10^{-4}$	0.003 69	0.134	94	$80 \times 10^6$	1.5	1.34	0.0
E	0.7700	0.4895	5.0	$5.66 \times 10^{-4}$	0.008 25	0.300	211	$10.6 \times 10^6$	1.0	5.33	0.0
F	0.0385	0.0245	0.25	$1.26 \times 10^{-4}$	0.001 85	0.067	47	$80 \times 10^6$	11.8	0.32	0.25

tailed examination of the effects of the initial conditions on the results lies outside the scope of the present study. The particle equation of motion [Eq. (4)] was solved in time for each particle using the second-order Adams–Bashforth scheme to compute the particle velocity. The fluid velocity,  $u_j$ , at the particle location which is needed to solve Eq. (4), was computed via a fourth-order accurate fully three-dimensional Hermite cubic interpolation polynomial. The particle position was then computed from the time integration of the particle velocity. In order to account for the effects of particles on the turbulence, the drag force acting on a particle  $p$  was linearly projected to the eight grid nodes surrounding the particle to compute  $f_{jp}$ , and  $f_j$  from Eq. (3). We tracked up to  $M_c=80 \times 10^6$  computational particles in our computational domain as shown in Table II in order to make the ratio,  $M_r/M_c$ , of the number of real to that of the computational particles as close to 1 as possible.

The computations were performed on 256 processors of the highly scalable supercomputer CRAY T3E. The computer program was written in FORTRAN 90 and parallelized with the Message Passing Interface (MPI) library. The particle-free simulation (case A) was the least expensive, requiring 1 CPU hour per processor and 8 GB of maximum total memory, whereas each of cases B,C,D, and F ( $M_c=80 \times 10^6$ ) required 11 CPU hours per processor and 58 GB of maximum total memory.

### III. RESULTS

#### A. Turbulence and particles parameters

We studied six cases to understand how particles with different inertia,  $\tau_p$ , modify the decay rate of isotropic turbulence in both zero- and finite-gravity conditions. The flow parameters are shown in Table I, and the particle properties are shown in Table II. Case A represents the particle-free flow, whereas cases B–E represent particle-laden flows with different inertia particles in zero gravity, and case F represents the particle-laden flow in *finite gravity*. All five cases (B–F) of particle-laden turbulence have the same volume fraction of particles,  $\phi_v=10^{-3}$ , and the same mass loading ratio  $\phi_m=1.0$  (for  $\rho_p/\rho=1000$ ). We only changed the particle diameter for each case to obtain a different ratio ( $\tau_p/\tau_k$ ) of the particle response time to the Kolmogorov time scale at the injection time, e.g.,  $\tau_p/\tau_k=0.1$  in case B, and  $\tau_p/\tau_k=5.0$  in case E. The effects of gravity are studied in case F where  $\tau_p/\tau_k=0.25$  (as in case C) and  $v_t/u_0^*=0.25$ , where  $v_t$  is the

terminal velocity ( $v_t=g\tau_p$ ) of the particle and  $u_0^*$  is the rms velocity of the surrounding fluid at the injection time, and gravity is in the negative  $x_3$  direction.

#### B. Turbulence modification by particles

In the following two subsections, Secs. III B 1 and III B 2, we describe briefly the temporal evolution of the turbulence kinetic energy, TKE, and its spectra,  $E(\kappa)$ , for all six cases (A–F). The detailed discussion of the physical mechanisms of the two-way interaction in these cases is presented in Sec. III C.

##### 1. Time evolution of turbulence kinetic energy

Figure 1 shows the temporal evolution of the turbulence kinetic energy normalized by its initial value,  $E(t)/E_0$ , for the zero gravity cases (A–E), and Fig. 2 shows the temporal development of the decay rate  $dE(t)/dt$  for the same cases. They show that microparticles (case B) with  $\tau_p/\tau_k < 0.25$  initially ( $1 < t \leq 2.1$ ) reduce the decay rate of TKE resulting in TKE being larger than that of case A at all times, whereas particles with higher inertia (critical particles, case D, and large particles, case E),  $\tau_p/\tau_k > 0.25$ , initially enhance the

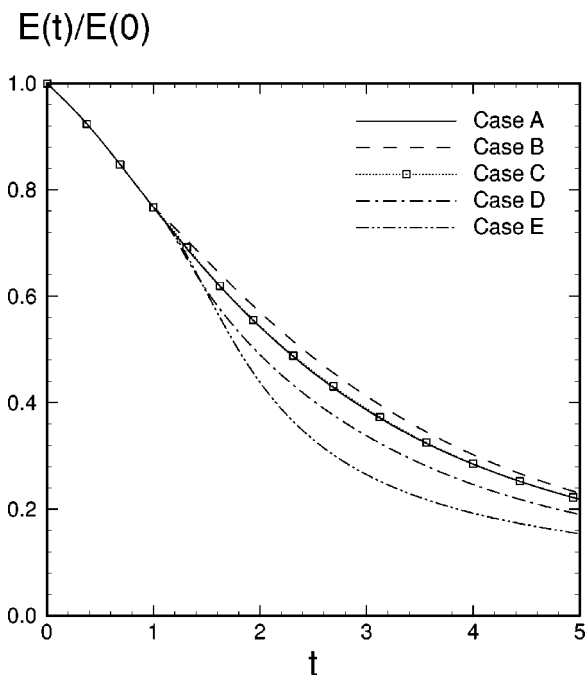
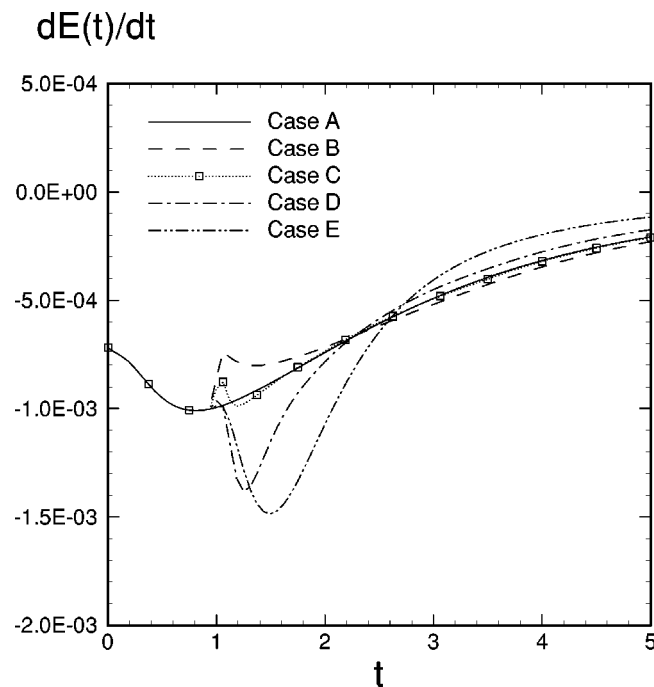


FIG. 1. Time development of the turbulence kinetic energy normalized by its initial value.

FIG. 2. Time development of the turbulence energy decay rate  $dE(t)/dt$ .

TKE decay rate considerably resulting in TKE being smaller than that of case A at all times. Figure 1 also shows that particles with  $\tau_p/\tau_k=0.25$  (case C) keep TKE nearly identical to that of case A at all times, with a percentage difference smaller than 0.6%. Thus, we denote the particles in case C “ghost” particles, since their effects on the turbulence cannot be detected by TKE’s temporal behavior,  $E(t)$ . However, as we will discuss later (Fig. 3) these ghost particles do modify the spectrum  $E(\kappa)$  of TKE. Figure 1 shows that at time  $t=5$ , in comparison to TKE in case A, TKE in case B is

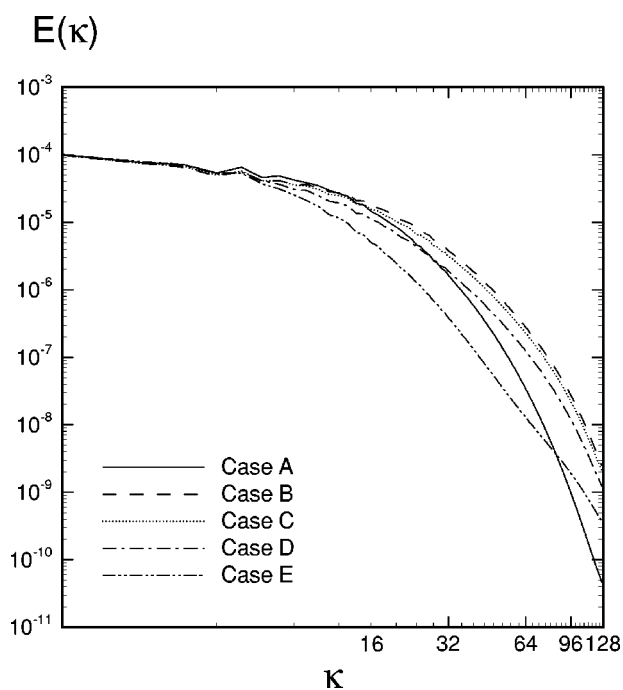
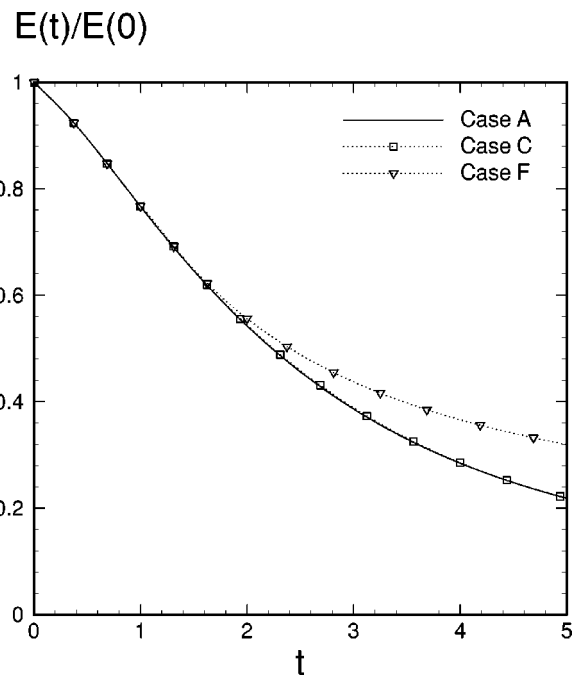
FIG. 3. Three-dimensional spatial spectrum of energy  $E(\kappa)$  at  $t=5.0$ .

FIG. 4. Time development of the turbulence kinetic energy normalized by its initial value.

larger by more than 5%; TKE in case C is nearly identical; TKE in case D is smaller by about 13%; and TKE in case E is smaller by about 30%.

Figure 4 displays the effects of gravity on the time evolution of TKE by comparing cases C and F. The figure shows that in presence of gravity (case F) particles reduce the decay rate of TKE as compared to both case C, the flow laden with ghost particles, and the particle-free flow, case A.

The basic physical mechanisms that are responsible for all the above-described modifications of  $E(t)$  by the dispersed particles are discussed in Sec. III C.

## 2. Energy spectrum

Figure 3 shows the three-dimensional energy spectra  $E(\kappa)$  for the five cases A–E at time  $t=5$ . Microparticles (case B) increase  $E(\kappa)$  relative to case A at wave numbers  $\kappa \geq 12$ , and reduce  $E(\kappa)$  relative to case A for  $\kappa < 12$ , such that  $\int E(\kappa) d\kappa \equiv$  TKE in case B is larger than in case A as shown in Fig. 1. For ghost particles (case C), although  $E(t)$  is nearly identical to that of case A at all times (Fig. 1), it is clear in Fig. 3 that the energy spectrum in case C differs from that in case A, but in such a unique way that its integral, TKE, is nearly identical to that of case A. Figure 3 shows that ghost particles reduce  $E(\kappa)$  relative to that of case A for  $\kappa < 15$ , and increase it above that of A for  $\kappa \geq 15$ . Critical particles (case D) increase  $E(\kappa)$  above that of case A for  $\kappa \geq 27$ , and reduce it for smaller wave numbers. In this case (D) the modulation of  $E(\kappa)$  is such that its integral, TKE, is smaller than in case A (Fig. 1). Large particles (case E) contribute to a faster decay of TKE by reducing the energy content at almost all wave numbers, except for  $\kappa > 87$ , where a slight increase of  $E(\kappa)$  occurs.

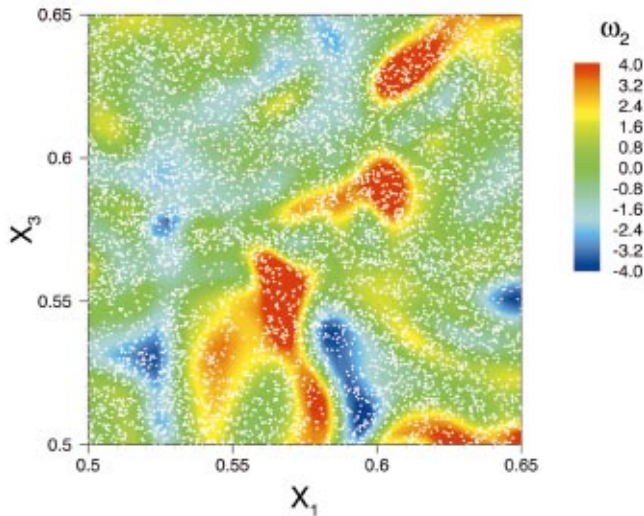


FIG. 5. (Color) Case B: microparticles (white dots) superimposed on  $\omega_2$  (color contour) at  $x_2=0.5$  and  $t=5.0$ .

In order to understand how the particles modify  $E(\kappa)$ , we write the evolution equation of the three-dimensional energy spectrum, derived in the Appendix [Eq. (A4)]

$$\frac{\partial E(\kappa)}{\partial t} = T(\kappa) - \varepsilon(\kappa) + \Psi_p(\kappa). \quad (7)$$

Equation (7) states that in particle-laden isotropic turbulent flows, the rate of change of spectral turbulence kinetic energy at wave number  $\kappa$  is the net result of the spectral energy-transfer rate  $T(\kappa)$  [Eq. (A5)], the spectral viscous dissipation rate  $\varepsilon(\kappa)$  [Eq. (A6)], and the spectral two-way coupling (fluid–particle drag interaction) energy rate  $\Psi_p(\kappa)$  [Eq. (A7)]. Discussion of the behavior of  $T(\kappa)$ ,  $\varepsilon(\kappa)$ , and  $\Psi_p(\kappa)$  and their effects on  $E(\kappa)$  is provided in the following section.

### C. Mechanisms of modification of isotropic turbulence by the particles

In this section we discuss the mechanisms responsible for the modification of decaying isotropic turbulence by the particles for the six cases listed in Table II. In zero gravity, microparticles ( $\tau_p/\tau_k \ll 1$ , case B) are analyzed in Sec. III C 1, large particles ( $\tau_p/\tau_k > 1$ , case E) in Sec. III C 2, critical particles with  $\tau_p/\tau_k \approx 1$  (case D) in Sec. III C 3, and ghost particles with  $\tau_p/\tau_k \approx 0.25$  (case C) in Sec. III C 4. In the presence of gravity, the behavior of ghost particles (case F) is analyzed in Sec. III C 5.

#### 1. Microparticles ( $\tau_p/\tau_k \ll 1$ )

*Microparticles* (case B) behave almost like flow tracers because their response time,  $\tau_p$ , is much smaller than the Kolmogorov time scale,  $\tau_k$ , but since their material density,  $\rho_p$ , is much higher than that of the carrier fluid,  $\rho$ , they cause the fluid to behave like a “heavy gas” (Saffman<sup>9</sup>).

In order to explain the physical mechanism of the two-way coupling, we write the time-evolution equation of TKE which is obtained by multiplying Eq. (1) by  $u_j$  and ensemble averaging

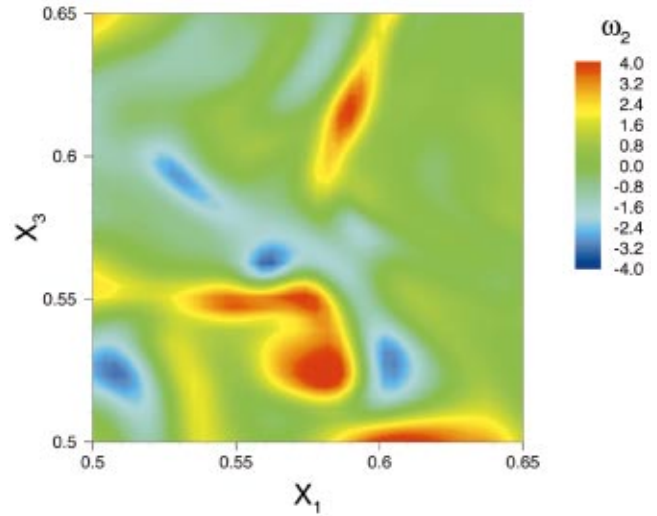


FIG. 6. (Color) Case A:  $\omega_2$  (color contour) at  $x_2=0.5$  and  $t=5.0$ .

$$\frac{dE(t)}{dt} = -\varepsilon(t) + \Psi_p(t), \quad (8)$$

where  $\varepsilon(t)$  is the viscous dissipation rate of  $E(t)$ , and  $\Psi_p(t)$  is the energy rate of change due to the particles drag force (Ahmed and Elghobashi<sup>10</sup>)

$$\Psi_p(t) = \phi_m \langle u_j (v_j - u_j) / \tau_p \rangle, \quad (9)$$

and  $\phi_m$  is the mass loading ratio ( $\phi_m = \phi_v \rho_p / \rho$ ).

Now, we show how the microparticles contribute to *both*  $\Psi_p(t)$  and  $\varepsilon(t)$ . Because of their fast response to the turbulent velocity fluctuations of the carrier flow, the microparticles are not ejected from the vortical structures of their initial surrounding fluid. Figure 5 shows contours of the instantaneous vorticity component  $\omega_2$  (in a small zone whose area is  $2.25 \times 10^{-2}$  of the vertical midplane,  $x_1 x_3$ , of our computational domain) and particles locations at  $t=5$  for case B. It is seen that the solid particles are not ejected from the vortex cores, and that the contours of maximum positive and negative values of vorticity occupy a larger fraction ( $\sim 18\%$ ) of that zone than in case A ( $\sim 9\%$ ) in Fig. 6. Furthermore, the inertia of the microparticles causes their velocity autocorrelation to be larger than that of their surrounding fluid ( $\langle v_j v_j \rangle > \langle u_j u_j \rangle$ , Fig. 7), indicating, as expected, that the microparticles retain their kinetic energy longer than the surrounding fluid. Since the microparticles’ trajectories are almost aligned with fluid points’ trajectories, and their kinetic energy is larger than that of their surrounding fluid, then the correlation  $\langle u_j v_j \rangle$  remains higher than the fluid velocity autocorrelation  $\langle u_j u_j \rangle$  (Fig. 7). Consequently,  $\Psi_p$  provides a positive contribution to  $dE(t)/dt$  in Eq. (8) as shown in Fig. 8, and hence  $\Psi_p$  is responsible for the reduction of the decay rate of TKE relative to case A.

On the other hand, the microparticles increase the viscous dissipation rate,  $\varepsilon(t)$ , relative to that of case A (Fig. 8). The reason is that microparticles remain in their initially surrounding vortices (Fig. 5), and the correlation  $\langle u_j v_j \rangle$  remains larger than  $\langle u_j u_j \rangle$  as discussed above, thus causing the vortical structures to retain their initial vorticity and strain rates

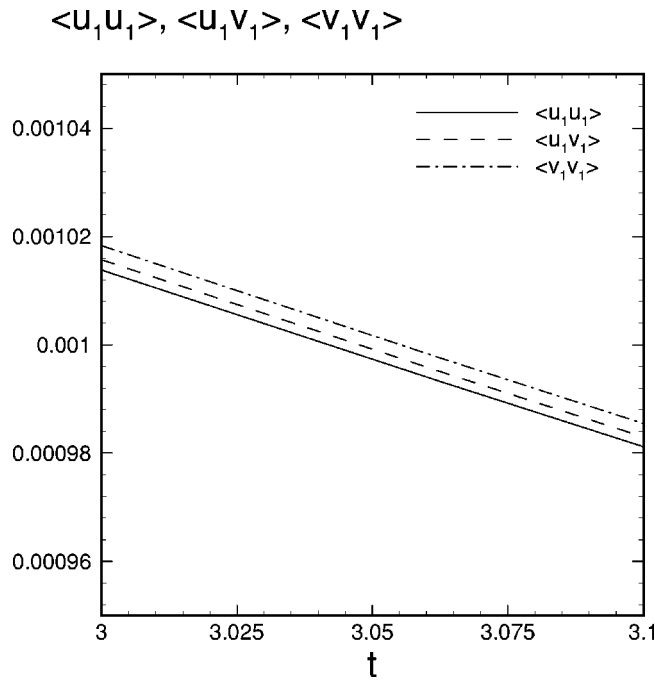


FIG. 7. Case B: time development of fluid velocity autocorrelation  $\langle u_1 u_1 \rangle$ , correlation  $\langle u_1 v_1 \rangle$  between the fluid velocity and particles velocity, and particle velocity autocorrelation  $\langle v_1 v_1 \rangle$ .

longer than the particle-free flow (case A). Table III shows that at time  $t=5$ , the enstrophy in case B is about 86% larger than that in case A. Table III also shows that the mean square of the strain rate

$$s_{ij} = (\partial u_i / \partial x_j + \partial u_j / \partial x_i) / 2, \tag{10}$$

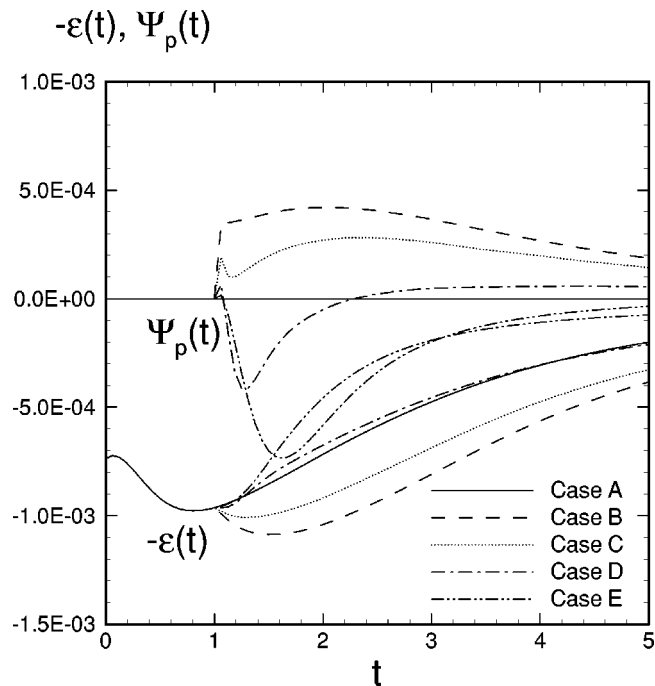


FIG. 8. Time development of the opposite of the energy dissipation rate  $-\varepsilon(t)$  and the fluid-particle drag interaction energy rate  $\Psi_p(t)$ .

TABLE III. Mean values of enstrophy and strain rate at time  $t=5$ .

Case	$\langle \omega^2 \rangle$	$\langle s_{ij} s_{ij} \rangle$
A—no particles	8.37	4.05
B—microparticles	15.6	7.26
C—ghost particles in zero gravity	13.1	6.20
D—critical particles	8.61	4.05
E—large particles	3.13	1.52
F—ghost particles in finite gravity	33.6	15.6

for case B is nearly 80% higher than that of case A at  $t=5$ . The square of the strain rate tensor is related to the three eigenvalues of  $s_{ij}$ , respectively the extensional ( $\alpha$ ), intermediate ( $\beta$ ), and compressive ( $\gamma$ ) strain rates ( $\alpha \geq \beta \geq \gamma$  and  $\alpha + \beta + \gamma = 0$  due to incompressibility), through the relation

$$s_{ij} s_{ij} = \alpha^2 + \beta^2 + \gamma^2. \tag{11}$$

At time  $t=5$ , Figs. 9–11 confirm that the values of  $\alpha$ ,  $\beta$ , and  $|\gamma|$  in case B are larger than in case A (i.e., the probability of finding a large value of  $\alpha$  is higher in case B than in case A). The viscous dissipation rate is related to the strain rates via

$$\varepsilon(t) = 2\nu \langle s_{ij} s_{ij} \rangle = 2\nu \langle \alpha^2 + \beta^2 + \gamma^2 \rangle, \tag{12}$$

and thus the viscous dissipation rate in case B is larger than in case A at all times as shown in Fig. 8. This increase of  $\varepsilon(t)$  is manifested in the reduction of the growth rate of the Kolmogorov time scale  $\tau_k(t)$  in Fig. 12. Figure 8 also shows that the magnitude of increase of  $\varepsilon(t)$  in case B relative to case A is less than the magnitude of  $\Psi_p(t)$  in the former, with the net result of a reduction in the decay rate of  $E(t)$  in case B according to Eq. (8) and shown in Fig. 1.

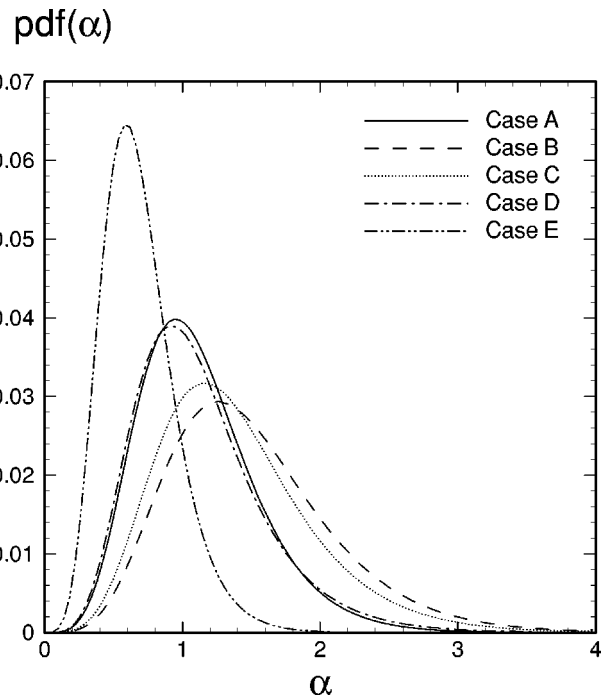


FIG. 9. Probability distribution of the principal extensional strain rate  $\alpha$  at  $t=5$ .

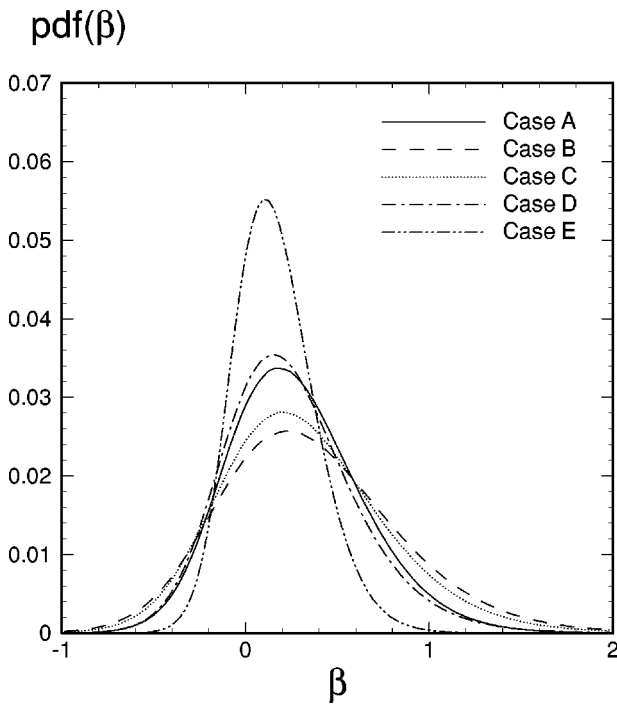


FIG. 10. Probability distribution of the principal intermediate strain rate  $\beta$  at  $t=5$ .

Now, we discuss the effects of the microparticles on the energy spectrum  $E(\kappa)$  (Fig. 3) of the carrier fluid. The time evolution of  $E(\kappa)$  is governed by Eq. (7). Microparticles contribute to *all* the terms on the right-hand side of Eq. (7) (Figs. 13–15). The time evolution of  $E(\kappa)$ , not shown here, indicates that the microparticles first modify the high wave number portion of the spectrum, before the smaller wave

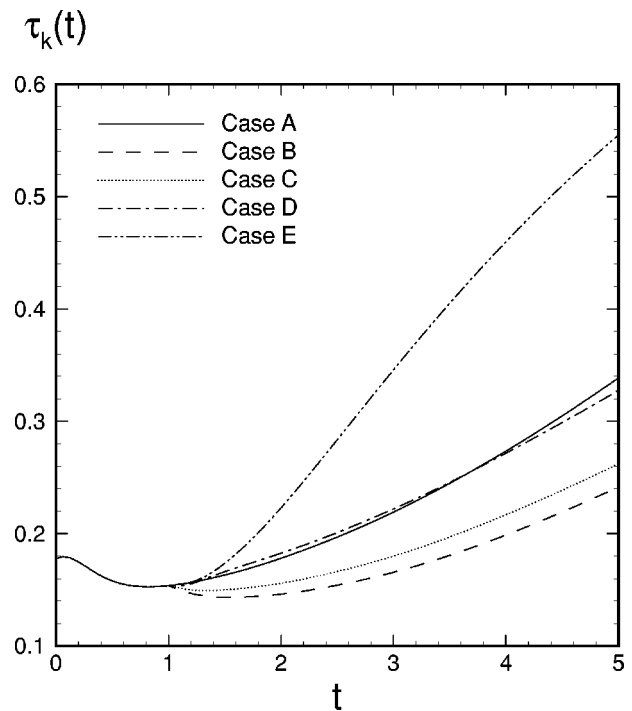


FIG. 12. Time development of the Kolmogorov time scale  $\tau_k = (\nu/\epsilon)^{1/2}$ .

numbers are affected as time increases. Because of their properties, microparticles ( $d \ll \eta$  and  $\tau_p \ll \tau_k$ ) directly interact with the small scales of motion, augmenting their energy content. The *triadic interaction of wave numbers* [Eq. (A5)] then alters the energy content of the other scales of motion, such that after few integral time scales,  $\tau_l$ ,  $E(\kappa)$  is modified at all the wave numbers as compared to the particle-free case (Fig. 3).

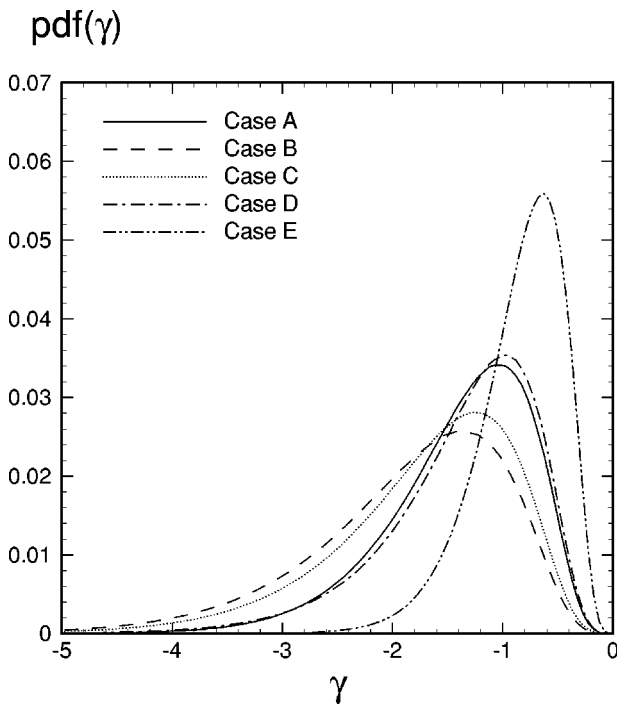


FIG. 11. Probability distribution of the principal compressive strain rate  $\gamma$  at  $t=5$ .

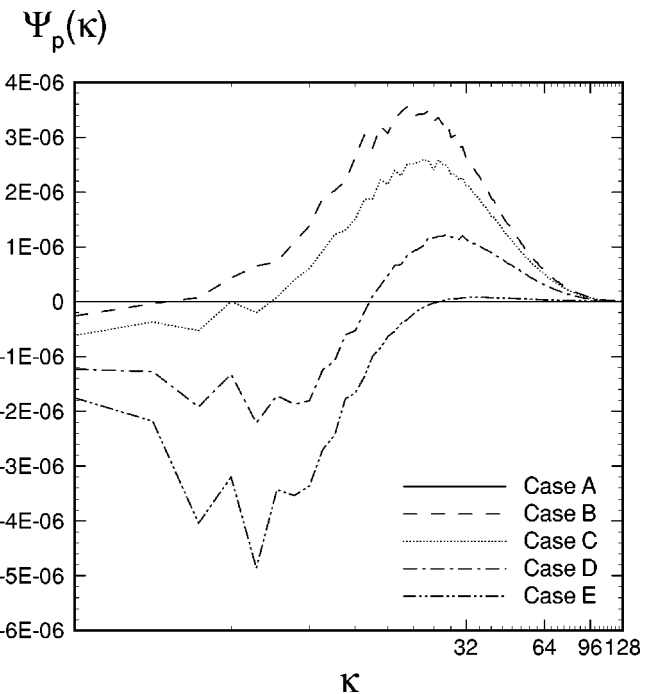


FIG. 13. Three-dimensional spatial spectrum of two-way coupling fluid-particles drag interaction energy rate  $\Psi_p(\kappa)$  at  $t=5.0$ .

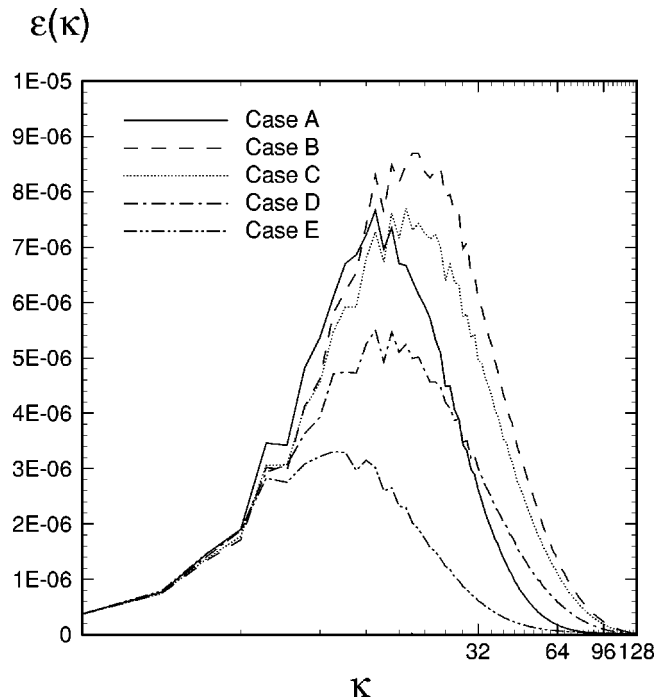


FIG. 14. Three-dimensional spatial spectrum of energy dissipation rate  $\varepsilon(\kappa)$  at  $t=5.0$ .

We have explained earlier in this section how microparticles produce a positive  $\Psi_p(t)$  (Fig. 8). Since  $\Psi_p(t) = \int \Psi_p(\kappa) d\kappa$  at time  $t$ , thus in case B this integral should be positive. Figure 13 shows that  $\Psi_p(\kappa)$  in case B is positive at almost all the wave numbers, and thus microparticles provide a positive two-way coupling contribution to  $\partial E(\kappa)/\partial t$  [Eq. (7)]. On the other hand, we have explained how the microparticles increase the dissipation rate,  $\varepsilon(t)$ , in case B as

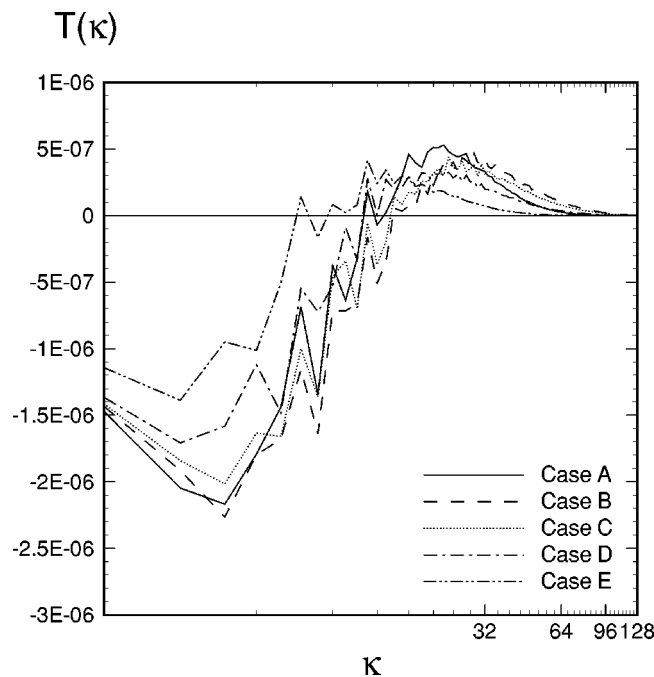


FIG. 15. Three-dimensional spatial spectrum of nonlinear energy transfer rate  $T(\kappa)$  at  $t=5.0$ .

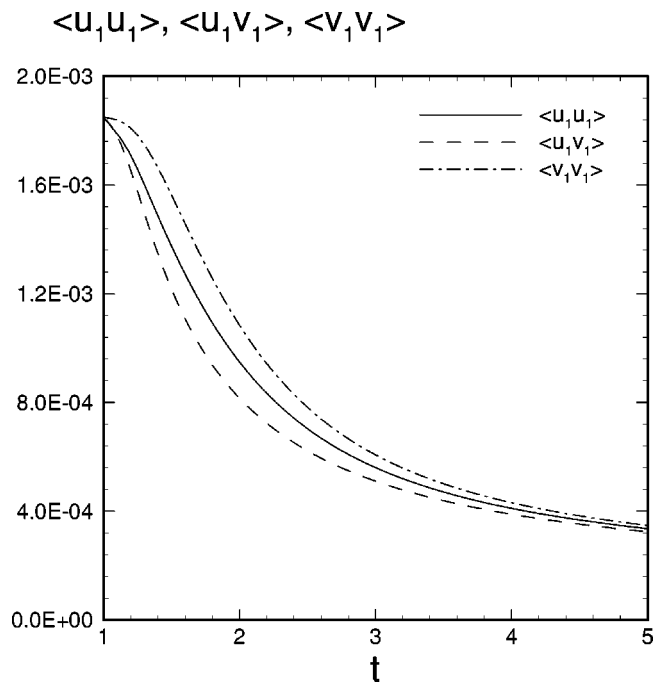


FIG. 16. Case E: time development of fluid velocity autocorrelation  $\langle u_1 u_1 \rangle$ , correlation  $\langle u_1 v_1 \rangle$  between the fluid velocity and particles velocity, and particle velocity autocorrelation  $\langle v_1 v_1 \rangle$ .

compared to the particle-free flow (Fig. 8). Since  $\varepsilon(t) = \int \varepsilon(\kappa) d\kappa$  at time  $t$ , thus  $\int \varepsilon(\kappa) d\kappa$  in case B should be larger than in case A (Fig. 14). Also  $\varepsilon(\kappa) = 2\nu\kappa^2 E(\kappa)$ , thus, in accordance with  $E(\kappa)$  in Fig. 3, Fig. 14 shows that  $\varepsilon(\kappa)$  in case B is larger than in case A at medium-high wave numbers. The increase of dissipation at high wave numbers causes a larger transfer rate of energy to the large  $\kappa$  from the small  $\kappa$ . The energy transfer rate  $T(\kappa)$  is thus modified, shifting the  $\kappa$  at which  $T(\kappa)=0$  towards higher wave numbers for case B as compared to case A (Fig. 15). Because of the increased transfer of energy from the small  $\kappa$ , the decay rate of  $E(\kappa)$  at small  $\kappa$  is increased, and thus  $E(\kappa)$  in case B is smaller than in case A at small  $\kappa$  (Fig. 3).

**2. Large particles ( $\tau_p/\tau_k > 1$ )**

*Large particles* (case E) here denote particles whose response time,  $\tau_p$ , is larger than the Kolmogorov time scale,  $\tau_k$ . Because of their large  $\tau_p$ , large particles do not respond to the velocity fluctuations of the surrounding fluid as quickly as microparticles do, but rather ‘escape’ from their initial surrounding fluid, “crossing” the trajectories of the fluid points (Yudine,<sup>11</sup> Elghobashi and Trusdell<sup>12</sup>). Whereas microparticles remain in the vortical structures of their initial surrounding fluid, large particles are “ejected” from these structures.

We now discuss how large particles modify both  $\Psi_p(t)$  and  $\varepsilon(t)$  to increase the decay rate of TKE (Fig. 2). Large particles retain their kinetic energy longer than their surrounding fluid does, thus resulting in  $\langle v_j v_j \rangle > \langle u_j u_j \rangle$ , as shown in Fig. 16. However, because of the “crossing trajectories” effects, the surrounding fluid velocity autocorrelation is larger than the correlation between particle velocity and

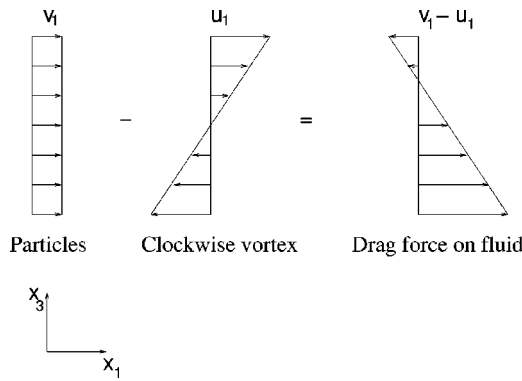


FIG. 17. Schematic of the drag interaction between large particles and a clockwise eddy ( $\omega_2 > 0$ ).  $-f_1 \propto (v_1 - u_1) \Rightarrow -\partial f_1 / \partial x_3 < 0$ .

fluid velocity,  $\langle u_j u_j \rangle > \langle u_j v_j \rangle$ , as shown in Fig. 16. Accordingly,  $\Psi_p(t)$  becomes negative [Eq. (9) and Fig. 8], and thus enhances the decay rate of TKE [Eq. (8), Figs. 1 and 2] at early times.

The effect of large particles on  $\varepsilon(t)$  is analyzed by examining how they modify the vorticity field. Figure 17 shows a schematic of the profile of the drag force imparted on the fluid when a group of large particles moving in the  $x_1$  direction interacts with a simple two-dimensional vortex in the  $x_1 x_3$  plane. The particle drag force [first term on the right-hand side of Eq. (4)] is proportional to the relative velocity  $(u_1 - v_1)$ . Thus, the effect of this interaction is to create a drag force on the fluid, in the  $x_1$  direction, whose gradient in the  $x_3$  direction is negative [recall that the net force exerted by the particles on the carrier fluid in the  $x_1$  direction is  $-f_1 \propto (v_1 - u_1)$ ]. This means that large particles interacting with a clockwise vortex create a counterclockwise torque on the fluid, which in turn reduces the vorticity. The fact that large particles contribute to a faster decay of vorticity can also be shown via the vorticity equation, obtained by taking the curl of the Navier–Stokes [Eq. (1)] equations

$$\frac{D\omega_i}{Dt} = \omega_k \frac{\partial u_i}{\partial x_k} + \nu \frac{\partial^2 \omega_i}{\partial x_k \partial x_k} + b_i, \quad (13)$$

where  $b_i = -\varepsilon_{ijk} \partial f_k / \partial x_j$  is the curl of the force field exerted by the particles on the fluid ( $-f_k$ ). Rewriting Eq. (13) for  $i=2$  to examine the two-dimensional vortex of Fig. 17, we obtain the evolution equation for  $\omega_2$

$$\frac{D\omega_2}{Dt} = \omega_k \frac{\partial u_2}{\partial x_k} + \nu \frac{\partial^2 \omega_2}{\partial x_k \partial x_k} - \frac{\partial f_1}{\partial x_3} + \frac{\partial f_3}{\partial x_1}. \quad (14)$$

Figure 17 shows that  $-\partial f_1 / \partial x_3 < 0$  for  $\omega_2 > 0$ . The last term in (14) vanishes since  $f_3 = 0$  as the particle motion is in  $x_1$  direction only. Thus, the decay rate of  $\omega_2$  is enhanced by the fluid–particle drag interaction. Table III shows at time  $t=5$  that the enstrophy in case E is nearly 63% smaller than in case A, and Fig. 18 shows that the maximum positive and negative values of  $\omega_2$  in case E are much smaller than in case A (Fig. 6), confirming the faster decay of vorticity caused by the presence of the large particles.

We have just shown that large particles reduce the lifetime of eddies; thus in case E the turbulence length- and time scales grow faster than in case A, in particular the Kolmog-

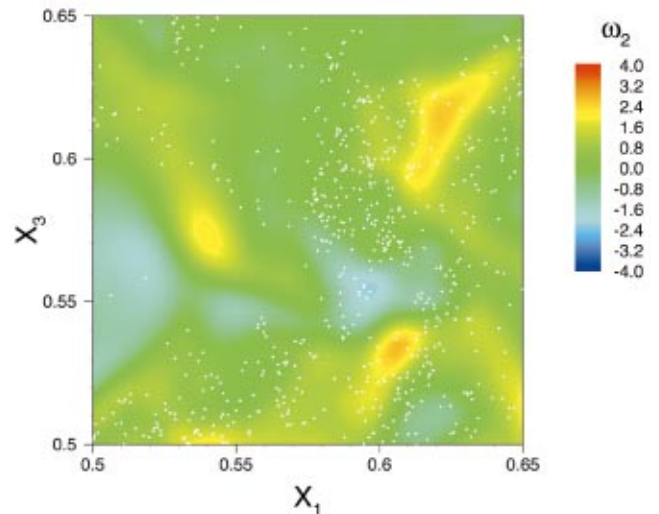


FIG. 18. (Color) Case E: large particles (white dots) superimposed on  $\omega_2$  (color contour) at  $x_2=0.5$  and  $t=5.0$ .

orov time scale  $\tau_{k_E}(t) > \tau_{k_A}(t)$  in Fig. 12. Consequently, the local velocity gradients in case E decay faster than in case A, and hence a faster decay of the magnitude of the local strain rate, defined in Eq. (10). Table III shows that the strain rate for case E is about 60% smaller than that of case A at  $t=5$ . Equation (11) shows that smaller local strain rate means smaller values of the strain rates  $\alpha$ ,  $\beta$ , and  $\gamma$ . Figures 9–11 confirm that, at time  $t=5$ , the values of  $\alpha$ ,  $\beta$ , and  $|\gamma|$  in case E are smaller than in case A. Thus, according to Eq. (12), the viscous dissipation rate in case E is smaller than that in case A at all times. Figure 8 shows that the magnitude of the negative  $\Psi_p(t)$  of case E is larger than the magnitude of the reduction of  $\varepsilon(t)$  relative to case A. The net result of these two opposing effects is the reduction of  $E(t)$  of case E relative to A at all times.

We now discuss the effects of the large particles on the energy spectrum  $E(\kappa)$  of the carrier fluid, Fig. 3. Large particles contribute to all the terms on the right-hand side of Eq. (7) for the time evolution of  $E(\kappa)$ , as seen in Figs. 13–15. We have explained earlier in this section how large particles produce a negative  $\Psi_p(t)$  in the physical space, Fig. 8. Figure 13 shows that  $\Psi_p(\kappa)$  in case E is negative at almost all the wave numbers, and thus the drag force of large particles represents a sink to  $\partial E(\kappa) / \partial t$  [Eq. (7)].

On the other hand, we have discussed how the large particles also reduce the dissipation rate,  $\varepsilon(t)$ , in case E as compared to the particle-free flow (Fig. 8). Figure 14 shows that  $\varepsilon(\kappa)$  in case E is smaller than in case A at nearly all wave numbers. The reduction of dissipation at medium-high wave numbers causes a reduction of the transfer rate of energy to the large  $\kappa$  from the small  $\kappa$ .  $T(\kappa)$  is thus modified as indicated by the shifting of the wave number at which  $T(\kappa)=0$  towards smaller  $\kappa$  for case E as compared to case A (Fig. 15). Thus, the modifications of both  $T(\kappa)$  and  $\varepsilon(\kappa)$  by large particles contribute to the reduction of the decay rate of  $E(\kappa)$ . The net result of the two opposing effects of  $\Psi_p(\kappa)$  on one side, and  $T(\kappa)$  and  $\varepsilon(\kappa)$  on the other, is the reduction

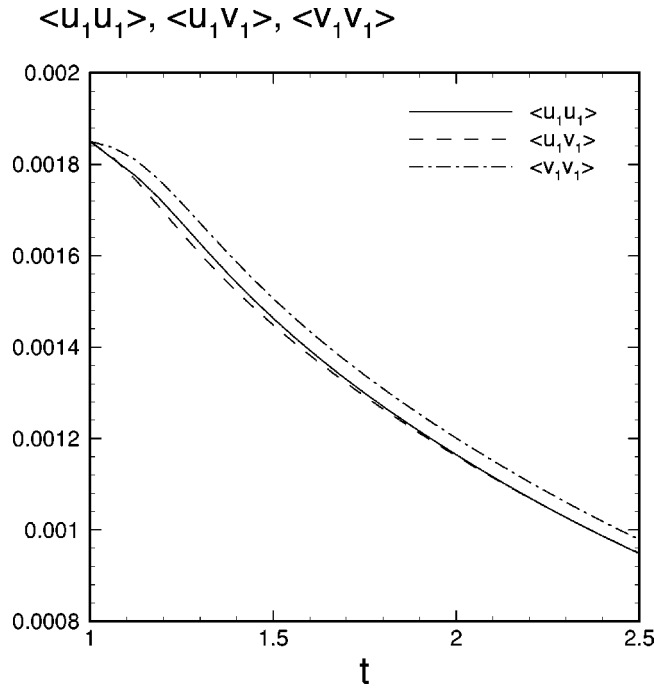


FIG. 19. Case D: time development of fluid velocity autocorrelation  $\langle u_1 u_1 \rangle$ , correlation  $\langle u_1 v_1 \rangle$  between the fluid velocity and particles velocity, and particle velocity autocorrelation  $\langle v_1 v_1 \rangle$ .

of  $E(\kappa)$  in case E at nearly all wave numbers relative to case A (Fig. 3).

### 3. Critical particles ( $\tau_p/\tau_k \approx 1$ )

We label the particles in case D ( $\tau_p/\tau_k = 1$ ) as “critical” particles because of their property of maximum preferential accumulation in comparison to other particles, as will be discussed later in this section. We will show that these particles are ejected from the large-vorticity cores of the eddies soon after injection, and remain in certain orbits (Fig. 22) not moving from one eddy into another as larger particles do (case E).

Now, we examine how these critical particles affect  $\Psi_p(t)$  and  $\varepsilon(t)$  to increase the decay rate of TKE with respect to case A (Fig. 1). For critical particles  $\Psi_p(t)$  is negative after injection (Fig. 8) and becomes positive at later times,  $t > 2.3 \approx t_{inj} + \tau_l = 1 + \tau_l$ , where  $\tau_l$  is the turnover time of the large scale motion (Table I). At early times ( $1 < t < 1 + \tau_l$ ) critical particles, as large particles, are centrifuged from their initial surrounding fluid and thus  $\langle u_j v_j \rangle < \langle u_j u_j \rangle$  as shown in Figs. 19 and 20. Consequently, according to Eq. (9)  $\Psi_p(t)$  becomes negative (Fig. 8) and thus contributes to the faster decay of TKE as compared to case A.

At later times ( $t > 1 + \tau_l$ ) after they have been “ejected” from the cores of vortices, the critical particles do not have sufficient inertia to cross the convergence regions (of high-speed fluid between the counter-rotating vortices) and enter new eddies, as large particles do, but rather accumulate in these regions of low vorticity and high strain (Maxey,<sup>13</sup> Wang and Maxey<sup>14</sup>). The occurrence of preferential accumulation can be indicated by the time development of the  $D_c$  factor (Wang and Maxey<sup>14</sup>), which measures the sum of the

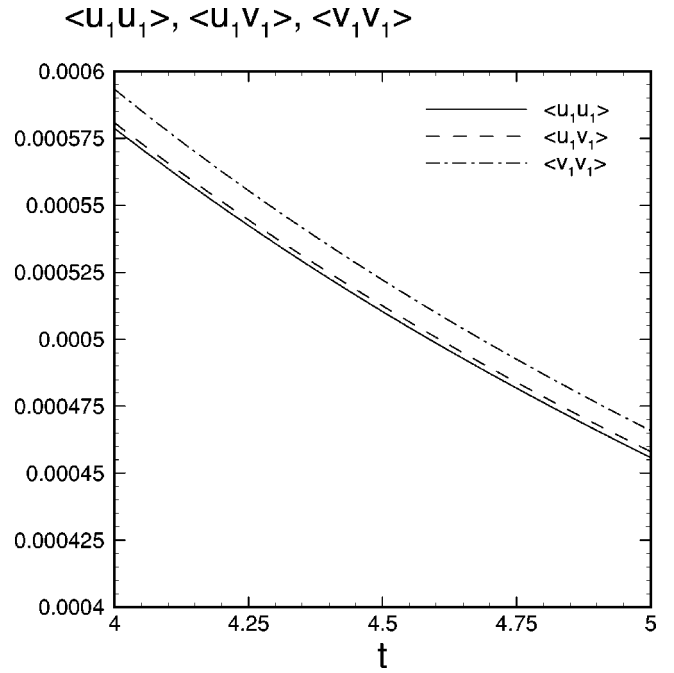


FIG. 20. Case D: time development of fluid velocity autocorrelation  $\langle u_1 u_1 \rangle$ , correlation  $\langle u_1 v_1 \rangle$  between the fluid velocity and particles velocity, and particle velocity autocorrelation  $\langle v_1 v_1 \rangle$ .

squared differences between the actual probability of concentration,  $P_c(C)$ , and the probability of random distribution,  $P_c^\mu(C)$ ,

$$D_c = \sum_{C=0}^{N_p} (P_c(C) - P_c^\mu(C))^2, \quad (15)$$

where  $N_p$  is the total number of computational particles (denoted  $M_c$  in Table II). The random distribution probability function is calculated as

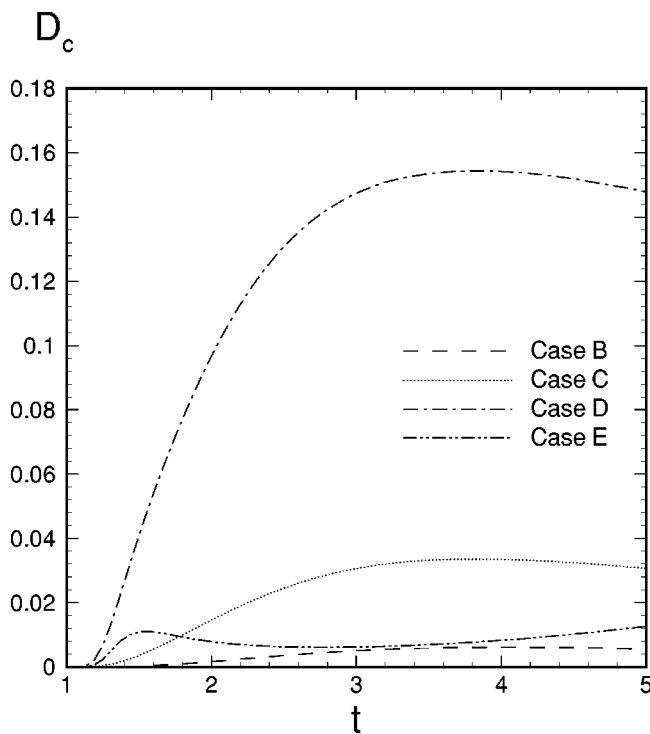
$$P_c^\mu(C) = \binom{N_p}{C} \left(\frac{1}{N_g}\right)^C \left(1 - \frac{1}{N_g}\right)^{N_p - C}, \quad C = 1, 2, \dots, N_p, \quad (16)$$

where  $N_g$  is the number of grid points of the computational domain [ $N_g = (256)^3$ ], and

$$\binom{N_p}{C} = \frac{N_p(N_p - 1) \dots (N_p - C + 1)}{C!}. \quad (17)$$

Figure 21 shows the time development of  $D_c$  for the four cases (B–E). It is clear that in case D (critical particles) the preferential accumulation is much larger than in the other three cases. Figure 22 clearly shows the preferential accumulation of the critical particles in orbits outside the regions of large  $\omega_2$ .

The higher inertia of the critical particles relative to the carrier fluid causes their velocity autocorrelation to be higher than that of the surrounding fluid,  $\langle v_j v_j \rangle > \langle u_j u_j \rangle$ , in Figs. 19 and 20, indicating that critical particles retain their kinetic energy longer than their surrounding fluid. Once these particles are in the high velocity convergence regions, characterized by pathlines of small curvature, their trajectories become more aligned with those of the fluid points. Con-


 FIG. 21. Time development of the  $D_c$  factor.

sequently the correlation  $\langle u_j v_j \rangle$  becomes larger than  $\langle u_j u_j \rangle$  for  $t > 1 + \tau_l$  (Fig. 20). Thus,  $\Psi_p(t)$  becomes positive [Eq. (9)] for  $t > 1 + \tau_l$  (Fig. 8). Since the high vorticity cores are nearly free of particles, then the two-way coupling force  $f_k \approx 0$  inside these cores, resulting in  $-\varepsilon_{ijk}(\partial f_k / \partial x_j) \approx 0$  in Eq. (13), and thus the evolution equation of vorticity reduces to that of particle-free flow. Table III confirms that the value of mean enstrophy at time  $t=5$  in case D is nearly equal to that of case A with a difference smaller than 3%.

Since the vortical structures in case D evolve nearly as in case A, the growth rates of the turbulence scales are nearly identical in both cases [ $\tau_{kD}(t) \approx \tau_{kA}(t)$  in Fig. 12]. Consequently, the decay rate of the local velocity gradients will be the same in both cases, resulting in a similar decay of the magnitude of the local strain rate. Table III shows that the strain rate for case D is identical to that of case A at  $t=5$ . At time  $t=5$ , Figs. 9–11 confirm that the values of  $\alpha$ ,  $\beta$ , and  $\gamma$  in case D are almost identical to those in case A. Accordingly, the viscous dissipation rates in these two cases are nearly the same (Fig. 8). Thus, the net effect of the modifications of  $\Psi_p(t)$  and  $\varepsilon(t)$  in case D (Fig. 8) is the reduction of  $E(t)$  relative to case A.

The modification of the energy spectrum  $E(\kappa)$  of the carrier flow by the critical particles (case D) is displayed in Fig. 3. It is seen that  $E(\kappa)$  for case D lies between those of case B (microparticles) and case E (large particles). Accordingly, the magnitudes of  $\Psi_p(\kappa)$ ,  $\varepsilon(\kappa)$  and  $T(\kappa)$  of case D are intermediate between those of cases B and E (Figs. 13–15).  $\Psi_p(\kappa)$  is positive at large  $\kappa$  as for microparticles, and negative at small  $\kappa$  as for large particles.  $\varepsilon(\kappa)$  is such that  $\varepsilon(t) = \int \varepsilon(\kappa) d\kappa$  is nearly identical to that of case A (Fig. 8) as discussed above. The net result of these modifications is

that in case D the crossover wave number of its  $E(\kappa)$  with that of the particle-free case (A) lies in between the crossover wave numbers of cases B and E.

#### 4. Ghost particles in zero gravity

It is clear from Fig. 1 and the discussion in the Secs. III C 1 and III C 3 that in comparison to the particle-free flow (case A), microparticles (case B,  $\tau_p / \tau_k = 0.1$ ) reduce the decay rate of TKE, and critical particles (case D,  $\tau_p / \tau_k = 1.0$ ) enhance that rate. These two opposing effects in cases B and D lead us to search for particles which have a “neutral” effect on that decay rate. More specifically, we searched for particles whose  $\tau_p$  is in the range  $0.1 < \tau_p / \tau_k < 1.0$  and which maintain the decay rate of TKE as that of the particle-free flow (case A). Our DNS results show that particles with  $\tau_p / \tau_k = 0.25$  (case C) satisfy this condition at all times, as shown in Figs. 1 and 2. Thus, we denote these particles as “ghost” particles because their presence in the flow cannot be detected by examining only the temporal development of TKE. It is important to emphasize that the value of  $\tau_p / \tau_k = 0.25$  is not universal, but depends on  $\text{Re}_{\lambda_0}$ ,  $\phi_m$ , and the magnitude of the gravitational acceleration (zero in our case). However, the significance of this finding is that dispersed particles are capable of modifying the turbulence energy spectrum (Fig. 3) in such a unique way that the amount of energy gained by the turbulence at high wave numbers balances exactly the amount of energy lost at low wave numbers, with the net result of retaining the integral of the spectrum equal to that of the particle-free flow at all times (Figs. 1 and 2).

Similar to microparticles, ghost particles are not ejected from the vortex cores (Fig. 23), and thus they enhance the lifetime of the vortical structures such that at time  $t=5$  the enstrophy and the strain rate in case C are larger than in case A by about 56% and 53%, respectively (Table III). Since ghost particles have larger inertia than microparticles, their trajectories tend to deviate from those of their surrounding fluid points more than the trajectories of microparticles do. Thus, the magnitudes of  $\Psi_p(t)$  and  $\varepsilon(t)$  for the ghost particles (Fig. 8) are smaller than those for the microparticles. However, the magnitudes of  $\Psi_p(t)$  and  $\varepsilon(t)$  for the ghost particles are in a “unique” proportion such that the positive  $\Psi_p(t)$  is just equal to the increase  $[\Delta \varepsilon(t)]$  in the magnitude of  $\varepsilon(t)$  with respect to case A, resulting in the net sum  $[\Psi_p(t) - \Delta \varepsilon(t)]$  being equal to  $\varepsilon(t)$  of case A. Consequently, the decay rate of TKE in case C is the same as in case A (Fig. 2).

#### 5. Ghost particles in finite gravity

In case F, we study the effect of gravity on the two-way coupling between the ghost particles of case C ( $\tau_p / \tau_k = 0.25$ ) and decaying isotropic turbulence. A gravitational acceleration is imposed in the negative  $x_3$  direction, and its magnitude is prescribed such that  $(v_i / u_0^*) = 0.25$  (Table II).

Figure 4 shows that due to gravity, the particles in case F reduce the decay rate of TKE relative to cases A and C at all times. Figure 24 compares the temporal developments of the three rms velocity components,  $u_{i,\text{rms}}(t)$  of the fluid in both

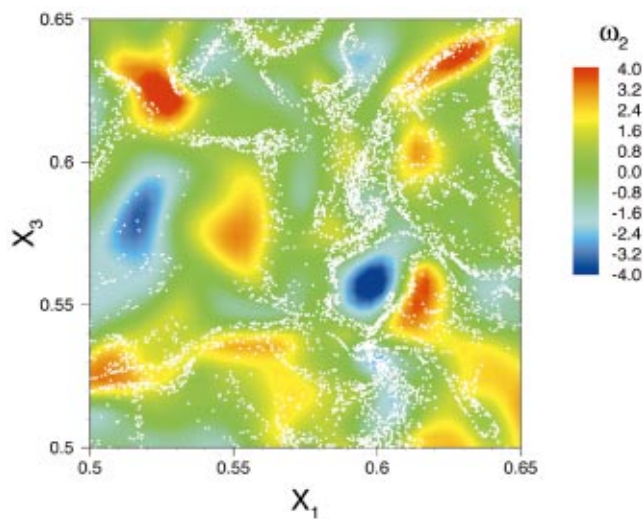


FIG. 22. (Color) Case D: critical particles (white dots) superimposed on  $\omega_2$  (color contour) at  $x_2=0.5$  and  $t=5.0$ .

cases A and F. It is seen that only the decay rate of the velocity component in the  $x_3$  direction,  $u_{3,rms}$ , has been considerably reduced relative to the other components, i.e., the two-way coupling in the presence of gravity in the  $x_3$  direction resulted in augmenting  $u_{3,rms}$ . The mechanisms responsible for this modulation will be discussed below by comparing the vorticity fields in cases C (zero gravity) and F (finite gravity).

Figures 23 and 25 display the contours of the instantaneous vorticity component  $\omega_2$  (in a small zone of the vertical midplane  $x_1x_3$  of our computational domain) and particles locations at  $t=5$  for cases C and F, respectively. We see that most of the vortical structures in case F are stretched in the  $x_3$  direction in a “banana-like” shape, and the values of maximum (positive and negative) vorticity are larger than in case C.

We also see that the particles in case F tend to accumulate in patches according to the mechanism of “preferential

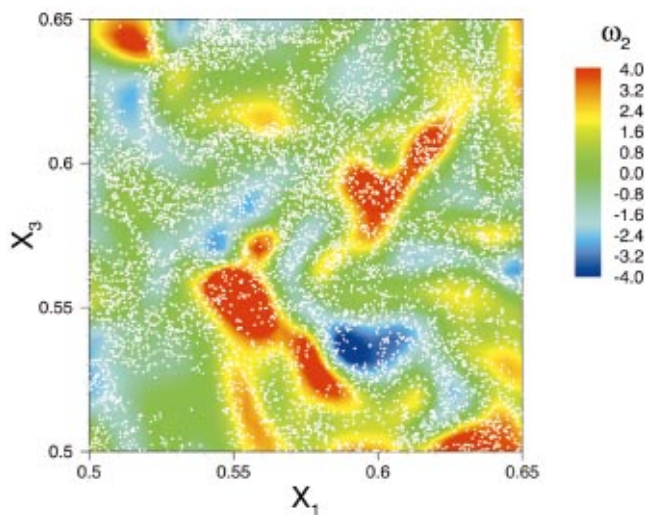


FIG. 23. (Color) Case C: ghost particles in zero gravity (white dots) superimposed on  $\omega_2$  (color contour) at  $x_2=0.5$  and  $t=5.0$ .

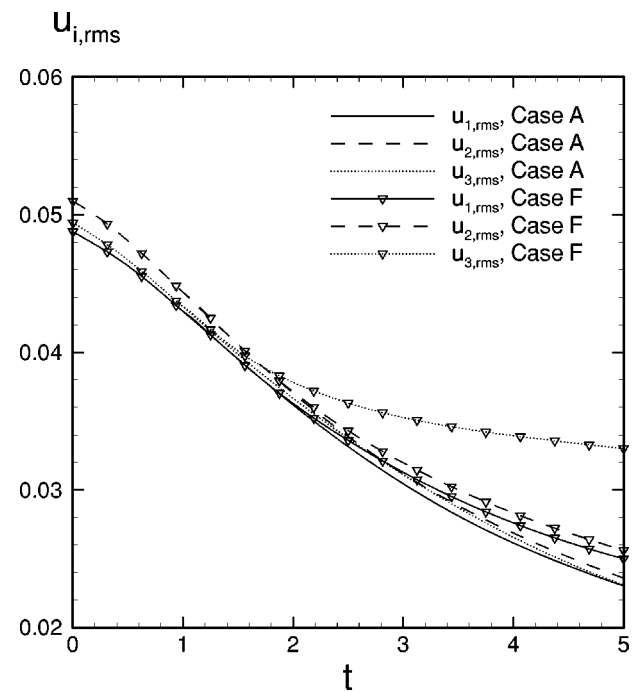


FIG. 24. Time development of rms fluid velocity components.

sweeping” described by Wang and Maxey.<sup>14</sup> The solid particles, settling under the effect of gravity, tend to follow a path where the local fluid instantaneous velocity is in the direction of gravitational acceleration (negative  $x_3$  direction). Figure 25 shows that the particles accumulate on the right side of a vortical structure with positive (clockwise) vorticity (red color) or on the left side of a structure with negative vorticity (blue color). This preferential accumulation/sweeping, as expected, creates zones that are nearly devoid of particles. Thus, *only* the side of the vortical structure swept by the trajectories of the particles will be subjected to a drag force,  $-f_3$ , directed downward. As a consequence of this asymmetry of the force acting on the fluid, local gradients  $\partial f_3/\partial x_1$  and  $\partial f_3/\partial x_2$  are generated in the horizontal

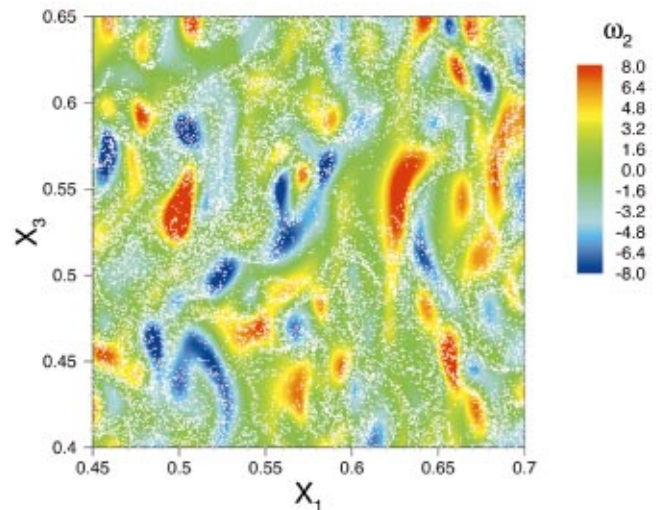


FIG. 25. (Color) Case F: ghost particles in finite gravity (white dots) superimposed on  $\omega_2$  (color contour) at  $x_2=0.5$  and  $t=5.0$ .

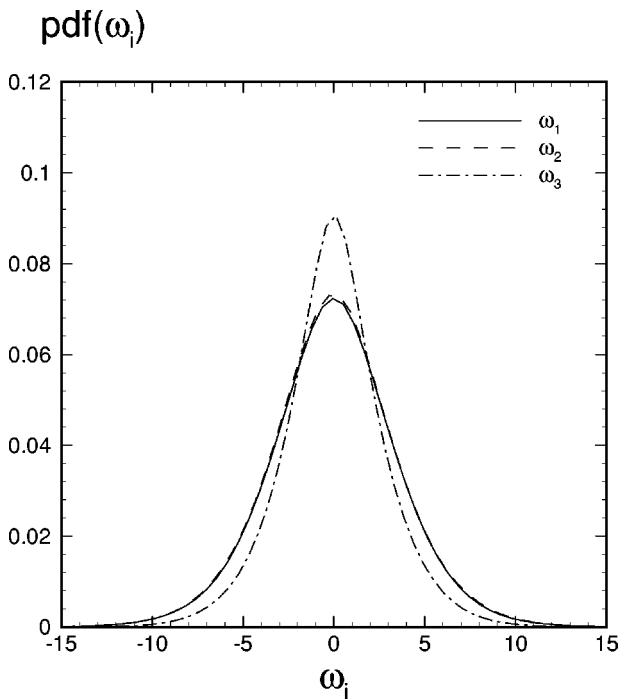


FIG. 26. Case F: probability density function of vorticity components  $\omega_i$  at  $t=5.0$ .

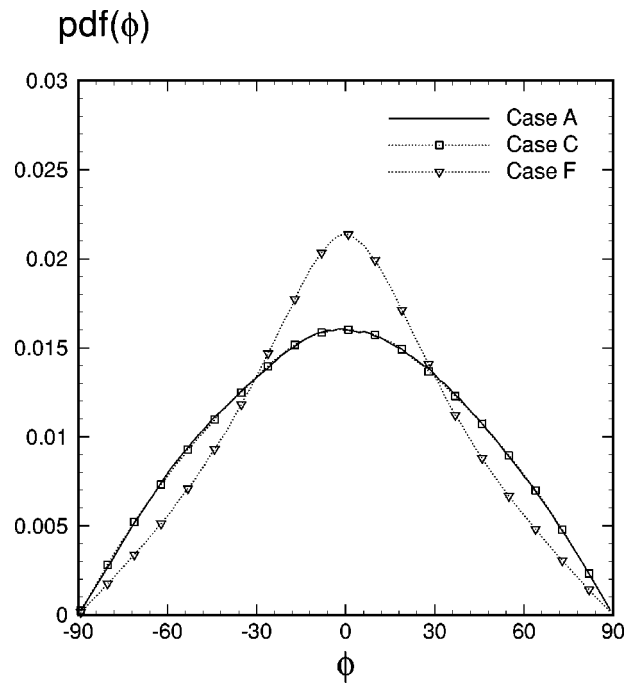


FIG. 27. Probability density function of the vorticity angle  $\phi$  at  $t=5.0$ .  $\phi$  is the angle between the vorticity vector and the horizontal plane  $x_1x_2$ .

plane, increasing the magnitudes of the source terms,  $b_i$ , of the horizontal components of vorticity,  $\omega_1$  and  $\omega_2$  [see Eqs. (13) and (14)], in addition to stretching the structures in the  $x_3$  direction. This physical behavior is confirmed in Fig. 26, which shows the pdf's of the three vorticity components at time  $t=5.0$  in case F. We observe higher probabilities for  $\omega_1$  and  $\omega_2$  than for  $\omega_3$  at larger values of  $\omega_i$ , thus explaining why  $u_{3,rms}$  is larger than  $u_{1,rms}$  and  $u_{2,rms}$  in Fig. 24. The anisotropy of the vorticity components is also indicated by the preferential alignment of the vorticity vector with the horizontal,  $x_1x_2$ , plane. Figure 27 shows that the pdf of the angle,  $\phi$ , between the vorticity vector and the horizontal plane  $x_1x_2$ , is larger in case F for  $\phi \approx 0$  relative to cases A and C, where the pdf of  $\phi$  has a normal distribution.

#### IV. SUMMARY

We have presented in the previous sections a detailed discussion of the physical mechanisms by which solid spherical particles, whose diameters are smaller than the Kolmogorov length scale, modify the structure of isotropic decaying turbulence. We classified the particles that we studied into four different categories based on the value of the ratio of their response time,  $\tau_p$ , to the Kolmogorov time scale of the carrier flow at the time of starting the particle trajectory calculation. We denote the particles whose  $\tau_p/\tau_k \ll 1$  as microparticles, those with  $\tau_p/\tau_k \approx 1$  as critical particles, and those with  $\tau_p/\tau_k > 1$  as large particles. In all the cases studied, both the volume fraction and mass fraction of the particles were fixed at  $\phi_v = 10^{-3}$  and  $\phi_m = 1$ , respectively. The different values of  $\tau_p$  were obtained by only changing the particle diameter.

We explained how microparticles reduce the decay rate of turbulence kinetic energy (TKE) and large particles enhance that rate as compared to particle-free turbulence. We then introduced ghost particles (whose  $\tau_p/\tau_k = 0.25$ ) which kept the decay rate of TKE nearly identical to that of particle-free turbulence by modifying the energy spectrum  $E(\kappa)$  in a unique way such that the energy gained by the turbulence at high wave numbers exactly balances the energy lost at small wave numbers. The two-way coupling effects in the above four cases, microparticles, large, critical, and ghost particles, were in zero-gravity conditions. We explained how the particles modify the carrier flow turbulence both in the physical and spectral spaces. We then studied the effects of finite gravity on the two-way coupling of ghost particles. The main findings can be summarized as follows.

- (1) Microparticles ( $\tau_p/\tau_k \ll 1$ ) remain in their initial surrounding vortices with their trajectories almost aligned with those of the initial fluid points, but with higher inertia. Thus, they allow the vortical structures to retain their initial vorticity and strain rates for longer time as compared to those of the particle-free flow. As a result, both the turbulence kinetic energy and the viscous dissipation rate are larger than those in particle-free turbulence at all times.
- (2) Large particles ( $\tau_p/\tau_k > 1$ ) escape from their initial surrounding fluid, and by crossing the trajectories of the fluid points, enter new eddies. The two-way coupling interaction (drag force) creates a torque on the fluid, counter to the local eddy's rotation, thus enhancing the decay rate of the vorticity as compared to the particle-free flow. Accordingly, the turbulence length- and time scales grow faster, and the turbulence kinetic energy and the strain rate decay faster than those in particle-free turbulence.
- (3) Critical particles ( $\tau_p/\tau_k \approx 1$ ), at early times after in-

jection ( $t_{inj} < t < t_{inj} + \tau_i$ ), are *ejected* from the cores of their initial surrounding vortices to peripheries of these vortices ( $\langle u_j v_j \rangle < \langle u_j u_j \rangle$ ), thus creating a negative  $\Psi_p(t)$ , which enhances the decay rate of TKE as compared to the particle-free flow. Consequently, the TKE in this case is smaller than in the particle-free case at all times. After the “ejection” process, critical particles do not enter new eddies, as large particles do, but rather *accumulate* in the convergence regions of the flow. Since the high vorticity cores are nearly free of particles the two-way coupling force is then nearly zero inside these cores, and thus they evolve like those of the particle-free flow. Consequently, the turbulence scales are nearly identical at all times to those in case A, and so are the enstrophy, the strain rate, and the viscous dissipation rate.

(4) Ghost particles in zero gravity ( $\tau_p/\tau_k=0.25$  for  $Re_{\lambda 0}=75$  and  $\phi_m=1$ ) cannot be detected, either experimentally or numerically, by examining only the temporal behavior of the turbulence kinetic energy, since they have a *neutral* effect on the decay rate of TKE compared to that of particle-free turbulence. However, they modify the turbulence energy spectrum in such a unique way that the amount of energy gained by the turbulence at high wave numbers balances exactly the amount of energy lost at low wave numbers, with the net result of retaining the integral of the spectrum equal to that of the particle-free flow at all times.

(5) Ghost particles in finite gravity ( $\tau_p/\tau_k=0.25$  and  $v_t/u_0^*=0.25$ ) through the mechanism of *preferential sweeping* (Wang and Maxey<sup>14</sup>) accumulate on the side of the vortical structures whose local instantaneous velocity has the same direction as the gravitational acceleration (negative  $x_3$  direction). Thus, only the side of the vortical structures directed downward is *swept* by the particles trajectories and subject to a drag force directed as gravity. In this configuration the particles stretch the vortical structures in the  $x_3$  direction in a *banana-like* shape, and, creating local gradients of the drag force ( $\partial f_3/\partial x_1$  and  $\partial f_3/\partial x_2$ ), increase the magnitudes of the source terms,  $b_i$ , of the horizontal components of vorticity,  $\omega_1$  and  $\omega_2$ . In turn, the flow becomes anisotropic because  $u_{3,rms}$  becomes larger than  $u_{1,rms}$  and  $u_{2,rms}$ , which explains the reduction of the decay rate of TKE as compared to the particle-free case. Further, the vorticity vector becomes preferentially aligned in the horizontal plane  $x_1x_2$ .

(6) In the spectral (Fourier) space, all particles modify the spectra of both  $T(\kappa)$  and  $\varepsilon(\kappa)$  in addition to creating  $\Psi_p(\kappa)$ .

**ACKNOWLEDGMENTS**

Preliminary results of this paper were presented at APS-DFD, 2001.<sup>15</sup> This work was supported by ONR Grant No. N00014-96-1-0213, and the computations were performed on CRAY T3E located at the Naval Oceanographic Office at NASA’s John C. Stennis Space Center, Mississippi.

**APPENDIX: EVOLUTION EQUATION OF THE SPECTRAL TURBULENCE KINETIC ENERGY  $E(\kappa)$  IN A PARTICLE-LADEN ISOTROPIC TURBULENT FLOW**

In order to derive the evolution equation for the three-dimensional energy spectrum  $E(\kappa)$  (time dependence is omitted for a more compact notation), we first need to perform the Fourier transformation of the Navier–Stokes [Eq. (1)] equations to obtain the evolution equation of the Fourier coefficient of velocity  $\hat{u}_j(\boldsymbol{\kappa})$

$$\frac{\partial \hat{u}_j(\boldsymbol{\kappa})}{\partial t} + \nu \kappa^2 \hat{u}_j(\boldsymbol{\kappa}) = -i \kappa_l P_{jk}(\boldsymbol{\kappa}) \sum_{\boldsymbol{\kappa}'} \hat{u}_k(\boldsymbol{\kappa}') \hat{u}_l(\boldsymbol{\kappa} - \boldsymbol{\kappa}') - \hat{f}_j(\boldsymbol{\kappa}), \tag{A1}$$

where “ $\hat{\phantom{x}}$ ” denotes Fourier transform, and

$$P_{jk}(\boldsymbol{\kappa}) \equiv \delta_{jk} - \frac{\kappa_j \kappa_k}{\kappa^2} \tag{A2}$$

is the projection tensor, with  $\delta_{jk}$  the Kronecker symbol,  $\hat{f}_j$  is the Fourier coefficient of  $f_j$ ,  $\boldsymbol{\kappa}$  is the wave number vector, and  $\kappa$  its magnitude. The evolution equation of the energy spectrum

$$E(\kappa) = \sum_{\kappa \leq |\boldsymbol{\kappa}| < \kappa+1} \frac{1}{2} [\hat{u}_j^*(\boldsymbol{\kappa}) \hat{u}_j(\boldsymbol{\kappa})], \tag{A3}$$

is obtained by multiplying each term of Eq. (A1) by  $\hat{u}_j^*(\boldsymbol{\kappa})$ , where “ $*$ ” denotes the complex conjugate, then sum the real part of each term over spherical shells of radius  $\kappa$  and thickness  $\Delta \kappa = 1$ . The resulting equation is

$$\frac{\partial E(\kappa)}{\partial t} = T(\kappa) - \varepsilon(\kappa) + \Psi_p(\kappa), \tag{A4}$$

where  $T(\kappa)$  is the spectral nonlinear energy-transfer rate to wave number  $\kappa$

$$T(\kappa) = \sum_{\kappa \leq |\boldsymbol{\kappa}| < \kappa+1} \kappa_l P_{jk}(\boldsymbol{\kappa}) \mathfrak{I} \left\{ \sum_{\boldsymbol{\kappa}'} \hat{u}_k(\boldsymbol{\kappa}') \hat{u}_l(\boldsymbol{\kappa} - \boldsymbol{\kappa}') \hat{u}_j^*(\boldsymbol{\kappa}) \right\}, \tag{A5}$$

$\varepsilon(\kappa)$  is the spectral viscous dissipation energy rate

$$\varepsilon(\kappa) = 2 \nu \kappa^2 E(\kappa), \tag{A6}$$

and  $\Psi_p(\kappa)$  is the spectral two-way coupling fluid-particle drag interaction energy rate,

$$\Psi_p(\kappa) = - \sum_{\kappa \leq |\boldsymbol{\kappa}| < \kappa+1} \Re \{ \hat{u}_j^*(\boldsymbol{\kappa}) \hat{f}_j(\boldsymbol{\kappa}) \}, \tag{A7}$$

where  $\Re\{\}$  and  $\mathfrak{I}\{\}$  denote the real and imaginary part.

<sup>1</sup>S. Elghobashi and G. C. Truesdell, “On the two-way interaction between homogeneous turbulence and dispersed solid particles. I. Turbulence modifications,” *Phys. Fluids A* **5**, 1790 (1993).

<sup>2</sup>K. D. Squires and J. K. Eaton, “Particle response and turbulence modification in isotropic turbulence,” *Phys. Fluids A* **2**, 1191 (1990).

- <sup>3</sup>M. Boivin, O. Simonin, and K. D. Squires, "Direct numerical simulation of turbulence modulation by particles in isotropic turbulence," *J. Fluid Mech.* **375**, 235 (1998).
- <sup>4</sup>S. Sundaram and L. R. Collins, "A numerical study of the modulation of isotropic turbulence by suspended particles," *J. Fluid Mech.* **379**, 105 (1999).
- <sup>5</sup>O. A. Druzhinin and S. Elghobashi, "On the decay rate of isotropic turbulence laden with microparticles," *Phys. Fluids* **11**, 602 (1999).
- <sup>6</sup>M. R. Maxey and J. Riley, "Equation of motion for a small rigid sphere in a turbulent fluid flow," *Phys. Fluids* **26**, 883 (1983).
- <sup>7</sup>T. Gerz, U. Shumann, and S. E. Elghobashi, "Direct numerical simulation of stratified homogeneous turbulent shear flows," *J. Fluid Mech.* **200**, 563 (1989).
- <sup>8</sup>U. Shumann, "Realizability of Reynolds-stress turbulence models," *Phys. Fluids* **20**, 721 (1977).
- <sup>9</sup>P. G. Saffman, "On the stability of laminar flow of a dusty gas," *J. Fluid Mech.* **13**, 120 (1962).
- <sup>10</sup>A. M. Ahmed and S. Elghobashi, "On the mechanism of modifying the structure of turbulent homogeneous shear flows by dispersed particles," *Phys. Fluids* **12**, 2906 (2000).
- <sup>11</sup>M. I. Yudine, "Physical consideration on heavy-particle diffusion," *Adv. Geophys.* **6**, 185 (1959).
- <sup>12</sup>S. Elghobashi and G. C. Truesdell, "Direct simulation of particle dispersion in a decaying isotropic turbulence," *J. Fluid Mech.* **242**, 655 (1992).
- <sup>13</sup>M. R. Maxey, "The gravitational settling of aerosol particles in homogeneous turbulence and random flow fields," *J. Fluid Mech.* **174**, 441 (1987).
- <sup>14</sup>L. P. Wang and M. R. Maxey, "Settling velocity and concentration distribution of heavy particles in homogeneous isotropic turbulence," *J. Fluid Mech.* **256**, 27 (1993).
- <sup>15</sup>A. Ferrante and S. Elghobashi, "On the decay rate of particle-laden isotropic turbulence," *Bull. Am. Phys. Soc.* **46**, 147 (2001).